Supporting information

Breaking the stability-activity trade-off in single-atom catalysis via interlayer electric fields in van der Waals heterostructure

Khayankhyarvaa Narmandakh, Suseong Hyun, Haeshik Lee, Byungchan Han[1*]

[1]Department of Chemical and Biomolecular Engineering, Yonsei University, Seoul 03722, Republic of Korea

*Corresponding author: bchan@yonsei.ac.kr

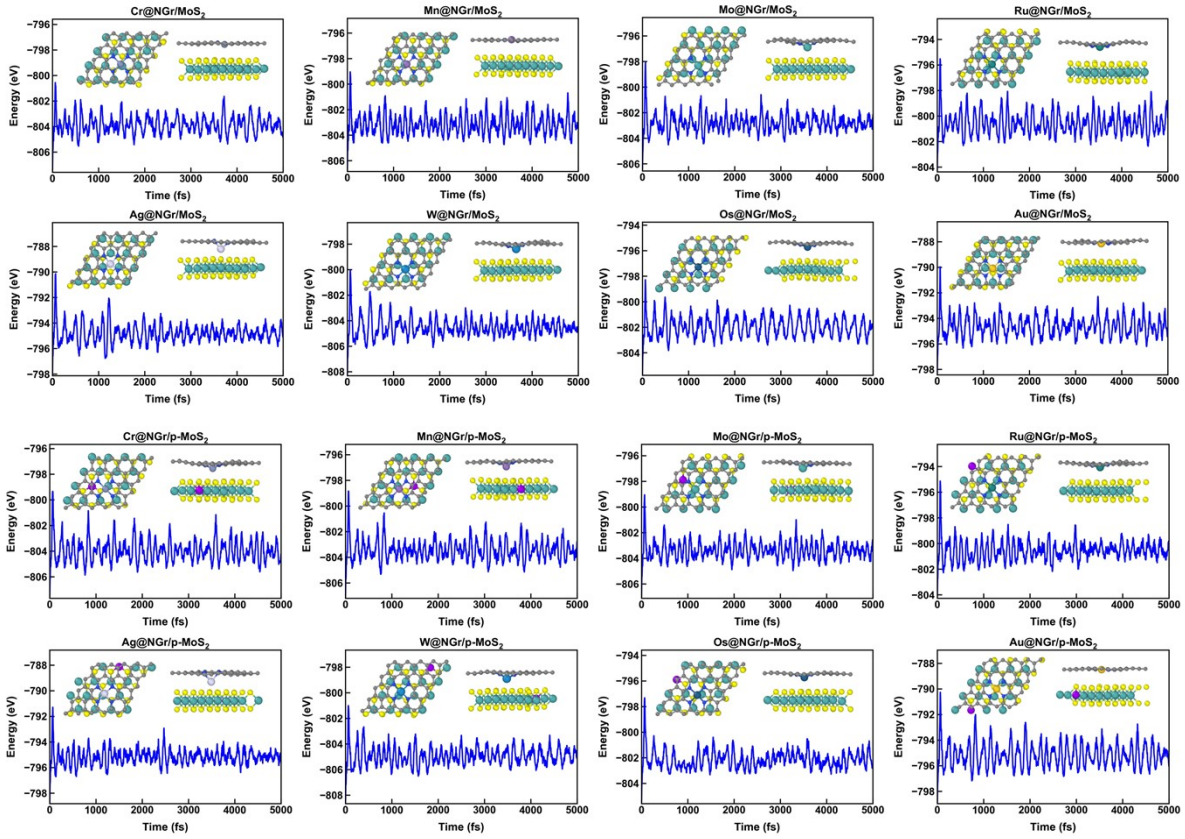

Figure S1. The AIMD simulation results for M@NGr/MoS_2 and M@NGr/p-MoS_2 structures. The inset displays the final structure after 5 ps. During the simulation, M@NGr and TMD layers moved in x and y directions, which is a normal phenomenon considering that the two layers interact with weak dispersion forces.

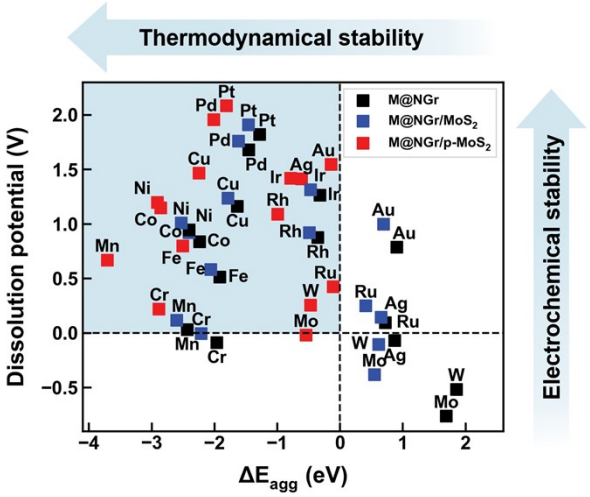

Figure S2. Stability map of all transition metal single atom in M@NGr, M@NGr/MoS_2, and M@NGr/p-MoS_2 structures illustrating resistance against aggregation and electrochemical dissolution. The blue quadrant denotes the optimal region where the single atom is both stable against aggregation and dissolution during HER in acidic conditions.

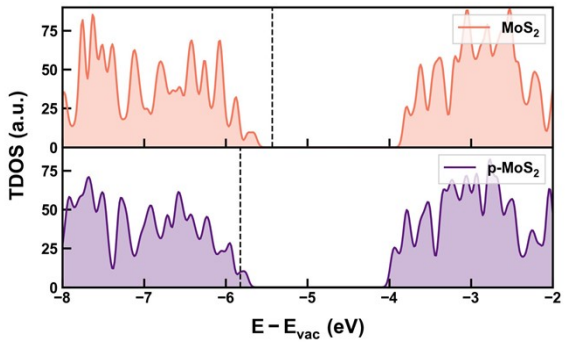

Figure S3. Total density of states (TDOS) of isolated monolayers of MoS_2 and Nb-doped p-type MoS_2 (p-MoS_2). The energies are referenced to the vacuum level (E_{vac}), and the dashed lines indicate the respective Fermi level (E_F) for each system. Nb doping shifts E_F to lower energy, increasing the work function of p-MoS_2 relative to undoped MoS_2 (5.82 eV vs. 5.43 eV; see Table S5) and thereby amplifying the work function mismatch with M@NGr upon heterostructure formation.

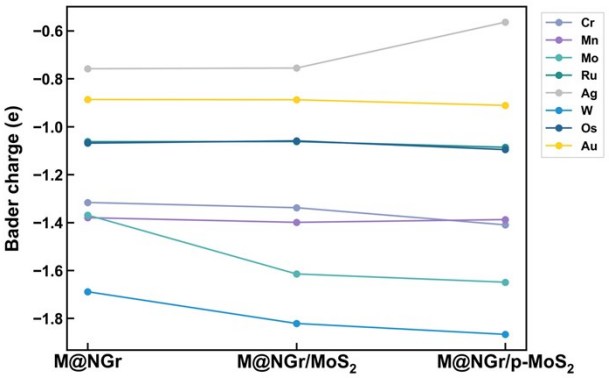

Figure S4. Bader charge of metal single atom in M@NGr, M@NGr/MoS_2, and M@NGr/p-MoS_2. The interfacial interactions do not significantly alter the charge state of metal atoms, suggesting that the interlayer charge transfer mainly occurs from C/N atoms in M@NGr to TMD.

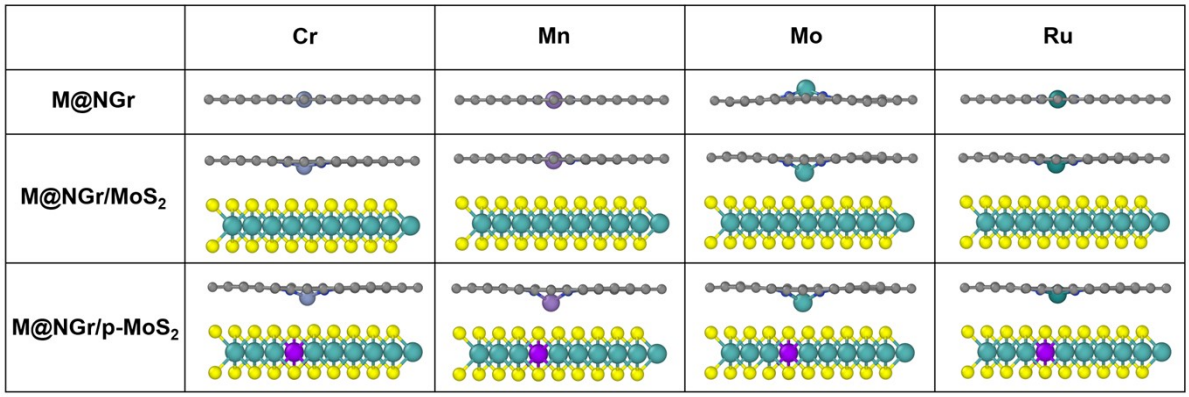

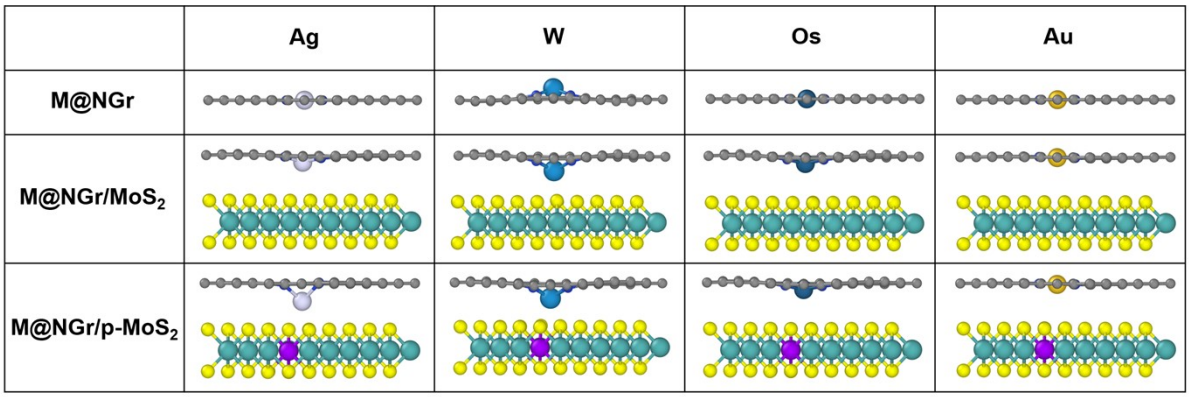

Figure S5. Side views of the DFT-optimized geometric structures of M@NGr, M@NGr/MoS_2, and M@NGr/p-MoS_2 for selected transition metals, showing the downward displacement (Δz) of the single metal atom along out-of-plane direction upon heterostructure formation. The progressive increase in Δz from M@NGr/MoS_2 to M@NGr/p-MoS_2 is consistent with the stronger built-in electric field and greater electrostatic attraction toward the TMD layer in the p-doped system. Color code: gray (C), blue (N), yellow (S), green (Mo), purple (Nb), and element-specific color for the single metal atom.

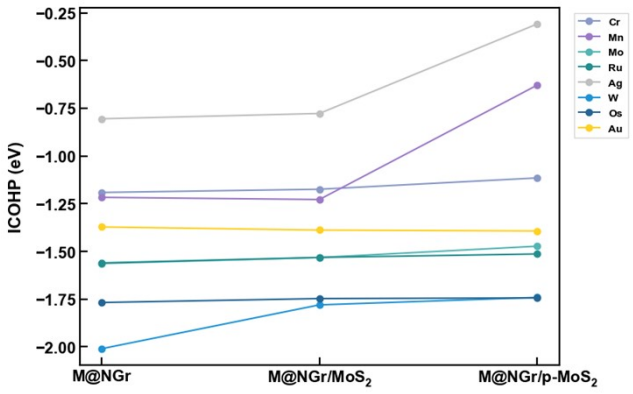

Figure S6. Integrated Crystal Orbital Hamilton Population (ICOHP) values for metal-N bond in M@NGr, M@NGr/MoS_2, and M@NGr/p-MoS_2, quantifying metal-N bond strength. The weakened ICOHP values are consistent with increased M-N bond lengths. For most metals, the M-N bond strengths remains nearly unchanged, showing that the enhanced single atom stability is not due to stronger M-N interactions but because of electrostatic attraction from interlayer built-in electric field.

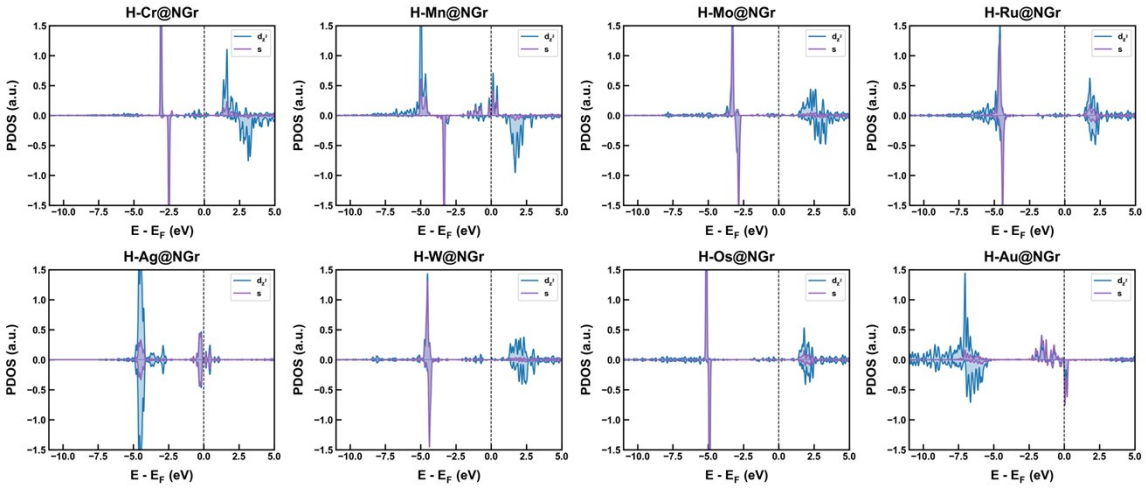

Figure S7. Projected density of states (PDOS) of the metal d_{z2} orbital and the adsorbed H 1s orbital in H-adsorbed M@NGr structures for all metals investigated. The energy levels of bonding and antibonding orbitals are consistent with the projected crystal orbital Hamiltonian populations (pCOHP) in Figure 6c.

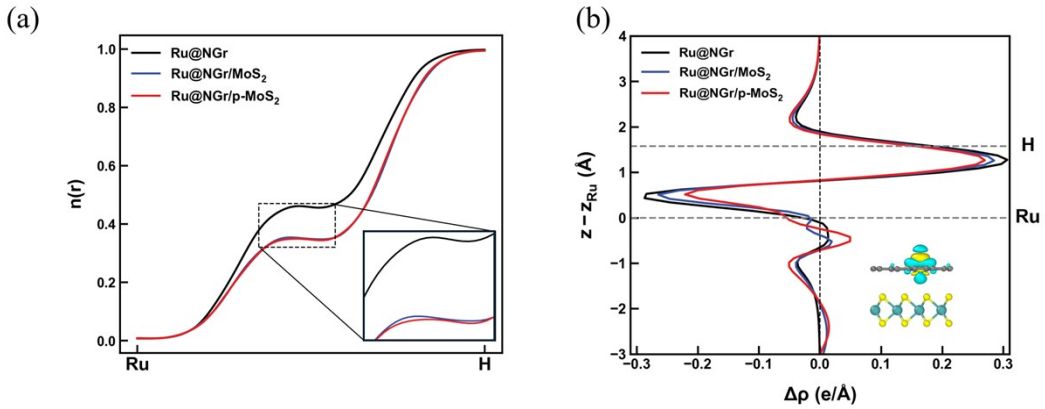

Figure S8. Charge redistribution and bonding character analysis of the Ru-H interaction in H-adsorbed Ru@NGr, Ru@NGr/MoS_2, and Ru@NGr/p-MoS_2. (a) Electron localization function (ELF) profiles computed along the line passing through the Ru-H bond axis, demonstrating the progressive reduction in covalency of Ru-H bonding upon heterostructure formation. (b) Plane-averaged and three-dimensional charge density difference ($\Delta\rho = \rho_{total} - \rho_{slab} - \rho_{H*}$) for each system (yellow: charge accumulation; cyan: charge depletion). The progressive attenuation of charge accumulation along the Ru-H axis from Ru@NGr to Ru@NGr/p-MoS_2 is consistent with the increasing Ru d_{z2} orbital delocalization induced by interlayer d_{z2}-p_z hybridization and weakening of the Ru-H covalent bond.

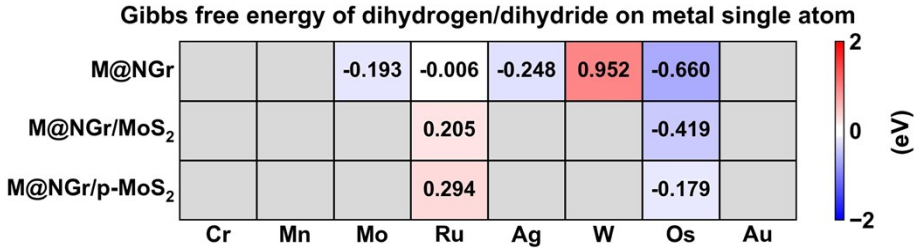

Figure S9. Free energy of dihydrogen/dihydride on metal single atoms in M@NGr, M@NGr/MoS_2, and M@NGr/p-MoS_2 systems. Shaded regions correspond to cases where H_2 was only weakly physisorbed with large metal-H distance.

Table S1. Optimized in-plane lattice parameters of graphene (Gr), and MoS_2 monolayers (unstrained and strained).

System	Lattice constant (Å)	Note
Gr	2.467	GGA-PBE optimized
MoS_2 (unstrained)	3.162	GGA-PBE optimized
MoS_2 (strained -2.47%)	3.084	Applied to match Gr supercell

Table S2. Aggregation energy (ΔE_{agg}) and single atom dissolution potential ($U_{diss,SAC}^{n+}$) values for all transition metal SACs in the M@NGr reference system used for Figure 2a, Figure 2b and Figure S2.

M	E_{coh}	E_{emb}	ΔE_{agg}	$U_{diss,bulk}^{n+}$			$U_{diss,SAC}^{n+}$		
				1+	**2+**	**3+**	**1+**	**2+**	**3+**
Cr	-4.150	-6.113	-1.963		-0.913	-0.744		0.068	-0.090
Mn	-2.920	-5.352	-2.432		-1.185	-0.276		0.031	0.535
Fe	4.320	-6.235	-1.915		-0.447	-0.037		0.511	0.601
Co	4.470	-6.703	-2.233		-0.280	0.453		0.836	1.198
Ni	4.480	-6.885	-2.405		-0.257			0.945	
Cu	3.510	-5.145	-1.635	0.521	0.342	1.028	2.156	1.159	1.573
Mo	-6.840	-5.445	1.395			-0.200			-0.665
Ru	-6.800	-6.074	0.726		0.455	0.386		0.092	0.144
Rh	5.760	-6.110	-0.350	0.600		0.758	0.950		0.875
Pd	3.930	-5.383	-1.453		0.951			1.678	
Ag	-2.960	-2.089	0.871	0.800	1.390	1.527	-0.071	0.955	1.236
W	-8.830	-6.975	1.855			0.100			-0.518
Os	-8.220	-7.271	0.949						
Ir	6.960	-7.277	-0.317			1.156			1.262
Pt	5.870	-7.148	-1.278		1.180			1.819	
Au	-3.830	-2.924	0.906	1.692	1.746	1.498	0.786	1.293	1.196

Table S3. Aggregation energy (ΔE_{agg}) and single atom dissolution potential ($U_{diss,SAC}^{n+}$) values for all transition metal SACs in M@NGr/MoS_2 structure used for Figure 2b and Figure S2.

M	E_{coh}	E_{emb}	ΔE_{agg}	$U_{diss,bulk}^{n+}$			$U_{diss,SAC}^{n+}$		
				1+	**2+**	**3+**	**1+**	**2+**	**3+**
Cr	-4.150	-6.360	-2.210		-0.913	-0.744		0.192	-0.007
Mn	-2.920	-5.521	-2.601		-1.185	-0.276		0.115	0.591
Fe	4.320	-6.376	-2.056		-0.447	-0.037		0.581	0.648
Co	4.470	-6.871	-2.401		-0.280	0.453		0.920	1.254
Ni	4.480	-7.008	-2.528		-0.257			1.007	
Cu	3.510	-5.294	-1.784	0.521	0.342	1.028	2.305	1.234	1.623
Mo	-6.840	-6.290	0.550			-0.200			-0.383
Ru	-6.800	-6.386	0.414		0.455	0.386		0.248	0.248
Rh	5.760	-6.247	-0.487	0.600		0.758	1.087		0.920
Pd	3.930	-5.543	-1.613		0.951			1.758	
Ag	-2.960	-2.303	0.657	0.800	1.390	1.527	0.142	1.061	1.307
W	-8.830	-8.214	0.616			0.100			-0.105
Os	-8.220	-7.581	0.639						
Ir	6.960	-7.427	-0.467			1.156			1.312
Pt	5.870	-7.325	-1.455		1.180			1.908	
Au	-3.830	-3.135	0.695	1.692	1.746	1.498	0.997	1.399	1.266

Table S4. Aggregation energy (ΔE_{agg}) and single atom dissolution potential ($U_{diss,SAC}^{n+}$) values for all transition metal SACs in M@NGr/p-MoS_2 structure used for Figure 2b and Figure S2.

M	E_{coh}	E_{emb}	ΔE_{agg}	$U_{diss,bulk}^{n+}$			$U_{diss,SAC}^{n+}$		
				1+	**2+**	**3+**	**1+**	**2+**	**3+**
Cr	-4.150	-7.032	-2.882		-0.913	-0.744		0.528	0.217
Mn	-2.920	-6.623	-3.703		-1.185	-0.276		0.666	0.958
Fe	4.320	-6.822	-2.502		-0.447	-0.037		0.804	0.797
Co	4.470	-7.325	-2.855		-0.280	0.453		1.147	1.405
Ni	4.480	-7.388	-2.908		-0.257			1.197	
Cu	3.510	-5.756	-2.246	0.521	0.342	1.028	2.767	1.465	1.777
Mo	-6.840	-7.379	-0.539			-0.200			-0.020
Ru	-6.800	-6.908	-0.108		0.455	0.386		0.509	0.422
Rh	5.760	-6.749	-0.989	0.600		0.758	1.589		1.088
Pd	3.930	-5.940	-2.010		0.951			1.956	
Ag	-2.960	-3.573	-0.613	0.800	1.390	1.527	1.413	1.696	1.731
W	-8.830	-9.296	-0.466			0.100			0.255
Os	-8.220	-8.045	0.175						
Ir	6.960	-7.743	-0.783			1.156			1.417
Pt	5.870	-7.676	-1.806		1.180			2.083	
Au	-3.830	-3.969	-0.139	1.692	1.746	1.498	1.831	1.816	1.544

Table S5. Calculated work functions of isolated MoS_2, p-MoS_2, and M@NGr monolayers for selected transition metals. Work functions were computed from the plane-averaged electrostatic potential using DFT-D3-corrected GGA-PBE+U functional. The consistently lower work functions of all M@NGr systems relative to MoS_2 and p-MoS_2 confirm that electrons flow from M@NGr to the TMD layer upon heterostructure contact for all metals investigated.

System	Work function (eV)
MoS_2	5.43
p-MoS_2	5.82
Cr@NGr	3.80
Mn@NGr	3.83
Mo@NGr	3.85
Ru@NGr	3.81
Ag@NGr	3.78
W@NGr	3.76
Os@NGr	4.03
Au@NGr	3.58

Table S6. Calculated magnetic moments (μ_B) of the single-atom metal center in M@NGr, M@NGr/MoS_2, and M@NGr/p-MoS_2. For Mn, heterostructure formation induces a low-spin to high-spin transition in M@NGr/p-MoS_2, driven by reduced crystal field splitting upon out-of-plane metal displacement. For Ag, the magnetic moment vanishes in M@NGr/p-MoS_2, indicating complete stabilization of the d^{10} closed-shell configuration upon Ag-N bond elongation. These element-specific spin-state responses provide supplementary stabilization contributions beyond the general electrostatic mechanism.

M	M@NGr (μ_B)	M@NGr/MoS_2 (μ_B)	M@NGr/p-MoS_2 (μ_B)	Spin state transition
Cr	3.575	3.545	3.453	—
Mn	3.262	3.293	4.441	Low spin→High-spin
Mo	2.925	2.166	2.295	—
Ru	1.645	1.597	1.623	—
Ag	0.441	0.413	0.000	High spin→Low-spin
W	1.816	1.478	1.598	—
Os	1.928	1.771	1.814	—
Au	0.000	0.000	0.000	—

Table S7. Average interlayer separation between the M@NGr layer and the top S plane of the TMD support, and the shortest M-S distance after structural relaxation. The interlayer separation is defined as the average height difference between the atoms in the M@NGr layer and the upper S atoms of the MoS_2 or p-MoS_2 layer. Underlined values denote M-S distances shorter than the sum of the corresponding covalent radii, indicating possible interfacial chemical bonding rather than purely vdW interaction.

M	Interlayer distance (Å)		M-S distance (Å)	
	M@NGr/MoS_2	M@NGr/p-MoS_2	M@NGr/MoS_2	M@NGr/p-MoS_2
Cr	3.38	3.35	3.12	2.71
Mn	3.40	3.38	3.42	2.52
Fe	3.40	3.41	3.45	3.36
Co	3.40	3.41	3.47	3.42
Ni	3.41	3.42	3.51	3.50
Cu	3.41	3.41	3.47	3.41
Mo	3.49	3.49	<u>2.41</u>	<u>2.46</u>
Ru	3.42	3.42	3.14	3.12
Rh	3.41	3.39	3.48	3.25
Pd	3.41	3.43	3.51	3.52
Ag	3.40	3.49	3.08	<u>2.38</u>
W	3.45	3.29	<u>2.35</u>	<u>2.55</u>
Os	3.48	3.45	3.16	3.16
Ir	3.41	3.43	3.52	3.55
Pt	3.41	3.43	3.52	3.55
Au	3.41	3.41	3.52	3.48